

Fragmentation with Discontinuous Galerkin schemes: Non-linear fragmentation

Maxime Lombart^{1*}, Mark Hutchison², Yueh-Ning Lee¹

¹*Department of Earth Sciences, National Taiwan Normal University, 88, Sec.4, Ting-Chou Road, Taipei 11677, Taiwan*

²*Universitäts-Sternwarte, Ludwig-Maximilians-Universität München, Scheinerstr. 1, 81679 München, Germany*

ABSTRACT

Small grains play an essential role in astrophysical processes such as chemistry, radiative transfer, gas/dust dynamics. The population of small grains is mainly maintained by the fragmentation process due to colliding grains. An accurate treatment of dust fragmentation is required in numerical modelling. However, current algorithms for solving fragmentation equation suffer from an over-diffusion in the conditions of 3D simulations. To tackle this challenge, we developed a Discontinuous Galerkin scheme to solve efficiently the non-linear fragmentation equation with a limited number of dust bins.

Key words: methods: numerical — (ISM:) dust, extinction

1 INTRODUCTION

Fragmentation resulting from collisions between grains is ubiquitous in astrophysics at all scales: asteroid belts (Williams & Wetherill 1994; Bottke et al. 2005), debris discs (Kenyon & Bromley 2004; Kobayashi & Tanaka 2010), protoplanetary discs (Safronov 1972; Birnstiel et al. 2016; Blum 2018), planetary rings (Brilliantov et al. 2015) and molecular clouds (Draine 2004; Jones 2004). Fragmentation counter-balances the coagulation process by forming small grains and maintaining a polydisperse dust size distribution. The role of dust grains is fundamental in many astrophysical processes: thermal emission (e.g. Draine 2004; Andrews 2020), formation of H₂ (e.g. Gould & Salpeter 1963; Jones 2021), dynamics (e.g. Testi et al. 2014; Lesur et al. 2022). Specifically large grains tend to decouple dynamically from the gas. For example in star formation, large grains preferentially accumulate in regions of high gas density (Lebreuilly et al. 2021). In protoplanetary discs, large grains drift radially inwards towards the star after losing momentum to the gas through drag (Whipple 1972; Weidenschilling 1977; Lesur et al. 2022, and references therein). Meanwhile, the acceleration of the gas by the dust, or "backreaction", is central to the operation of the streaming instability (Youdin & Goodman 2005; Testi et al. 2014; Jaupart & Laibe 2020; Lesur et al. 2022, and references therein) and, consequently, planetesimal formation (Gonzalez et al. 2017). All these physical processes emphasise the importance of accounting for the evolution of the dust size distribution at all scales in astrophysics.

Key to understanding the impact of dust on the interstellar medium (ISM) and protoplanetary discs is the knowledge of how the complete dust size distribution evolves in time. This study focuses on the non-linear fragmentation (Cheng & Redner 1990; Kostoglou & Karabelas 2000; Ernst & Pagonabarraga 2007; Pagonabarraga et al. 2009) that occurs when two grains collide, which plays an important

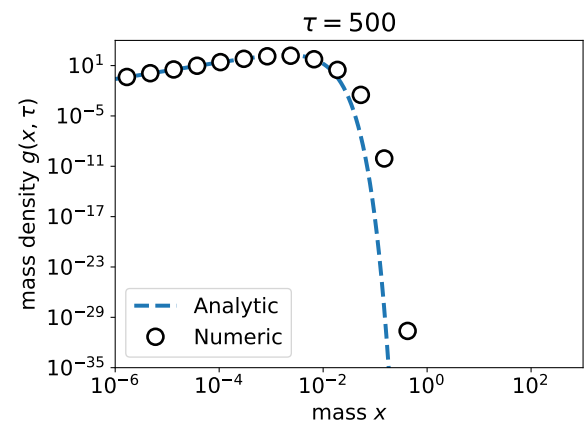


Figure 1. Numerical diffusion problem for fragmentation: numerical schemes of order 0 over-estimate the mass density of large grains at low resolution, here for the case of a non-linear fragmentation equation with multiplicative collision kernel and $N = 20$ logarithmically-spaced dust bins.

role in maintaining the small grain population in astrophysical environments. This fragmentation model is distinct from the linear fragmentation model where the breakup of grains is driven spontaneously by external forces where dust collisions are rare (Cheng & Redner 1990; Kostoglou & Karabelas 2000). Details of this model are given in Appendix A. The non-linear fragmentation models the breakup of grains of any size. The non-linear fragmentation process is formalised within the framework of Smoluchowski-like equation by the mean-field non-linear fragmentation equation (Redner 1990; Kostoglou & Karabelas 2000; Ernst & Pagonabarraga 2007; Pagonabarraga et al. 2009; da Costa 2015; Banasiak et al. 2019). The non-linear fragmentation equation does not have generic analytic solutions but its mathematical description is linked to the linear fragmentation equation (e.g. Redner 1990; Kostoglou & Karabelas 2000; Ernst & Pagonabarraga 2007; Pagonabarraga et al. 2009; Paul & Kumar 2018; Barik & Giri 2018; Das et al. 2020). For

* maxime.lombart@gapps.ntnu.edu.tw

astrophysics problems, the non-linear fragmentation equation has to be solved numerically.

Dust evolution (i.e. coagulation and fragmentation) is important at many different scales in astrophysics, from the ISM to planet formation (e.g. [Safronov 1972](#); [Tanaka et al. 1996](#); [Bottke et al. 2005](#); [Brauer et al. 2008](#); [Hirashita & Yan 2009](#); [Ormel et al. 2009](#); [Kobayashi & Tanaka 2010](#); [Brilliantov et al. 2015](#); [Blum 2018](#); [Jones 2021](#)). Tracking the size evolution of dust in 3D simulations of these environments would be a big step forward, but is currently hindered by the lack of numerical schemes that are both economical and accurate – particularly in the case of non-linear fragmentation where large grains fragments into small grains. For example, Fig. 1 illustrates the over-diffusion problem for fragmentation commonly seen numerical schemes of order 0 with insufficient mass resolution (shown here with 20 bins). The mass density of large grains becomes increasingly inaccurate with time, which later impacts the evolution of small grains. Brute force has been the standard approach to combating over diffusion in the past – typically employing hundreds of mass bins to maintain accuracy. In comparison, 3D hydrodynamical simulations can feasibly only accommodate a few tens of bins, making the two methods incompatible. Inspired by the recent work of [Liu et al. \(2019\)](#) and [Lombart & Laibe \(2021\)](#), we took a different approach to modelling the non-linear fragmentation equation that significantly closes this computation gap. Using a high-order solver based on the Discontinuous Galerkin method we found we could reduce the number of mass bins without sacrificing accuracy. Our goal in this paper is to apply these same methods to the non-linear fragmentation equation.

The structure of the paper is as follows: Properties of the non-linear fragmentation equation discussed in the astrophysical context are presented in Sect. 2. The Discontinuous Galerkin numerical scheme is presented in Sect. 3. The performance of the solver regarding the over-diffusion problem are studied in Sect. 4. Applicability of the algorithm in astrophysical and other contexts are discussed in Sect. 5.

2 NON-LINEAR FRAGMENTATION EQUATION

The non-linear fragmentation equation describes the mass distribution of grains where mass transfers from large to small grains. The fragmentation process is modelled by a non-linear partial integro-differential hyperbolic equation that depends on two quantities: i) the fragmentation kernel, which describes the collision rate between two grains, and ii) the distribution of outgoing fragments. Specifically, this non-linear fragmentation model considers that only one of the two colliding grains breaks-up (see Sect. 2.3), which is the case for a collision between a large and a small grains. The non-linear fragmentation equation was initially formalised in fields of chemistry and atmospheric science ([Kostoglou & Karabelas 2000](#), and references therein). Explicit solutions exist only for simple forms of the fragmentation kernel, such as the constant and multiplicative kernels, and the distribution of fragments ([Ziff & McGrady 1985](#); [McGrady & Ziff 1987](#); [Kostoglou & Karabelas 2000](#); [Ernst & Pagonabarraga 2007](#)). Many of the analytic solutions are similar to the linear case ([Kostoglou & Karabelas 2000](#)) and share properties, such as self-similarity and shattering ([McGrady & Ziff 1987](#); [Cheng & Redner 1988, 1990](#); [Kostoglou & Karabelas 2000](#); [Ernst & Pagonabarraga 2007](#)). In astrophysics, collisions leading to fragmentation occur mainly through ballistic impacts ([Safronov 1972](#); [Tanaka et al.](#)

[1996](#); [Dullemond & Dominik 2005](#); [Kobayashi & Tanaka 2010](#)), for which no analytical solutions exist and require numerical solutions.

2.1 Conservative form

The non-linear fragmentation equation was formalised in a mean-field approach by [Kostoglou & Karabelas \(2000\)](#). Fragments are assumed to be spherical. Spatial correlations are neglected. For physical systems involving the fragmentation of aggregates made of a large number of monomers, it is convenient to assume a continuous mass distribution. The population density of grains within an elementary mass range dm is characterised by its number density $n(m)$. The continuous collisional fragmentation equation is given by

$$\begin{aligned} \frac{\partial n(m, t)}{\partial t} = & \int_0^\infty \int_m^\infty K(m', m'') b(m, m'; m'') n(m', t) n(m'', t) dm' dm'' \\ & - n(m, t) \int_0^\infty K(m, m') n(m', t) dm', \end{aligned} \quad (1)$$

where t denotes time, m' and m'' the masses of two colliding grains, m the mass of fragments and $n(m, t)$ is the number density function by mass unit of particles of mass m . The first term on the right-hand side of Eq. 1 represents the increase of particle of mass m produced by the fragmentation of a particle of mass m' due to collision with a particle of mass m'' (breaking of a large particle to form an orange particle in Fig. 2). The averaged probabilities of collision leading to fragmentation are encoded inside the fragmentation kernel $K(m', m'')$, which is a symmetric function of m' and m'' for binary collisions. The second term of Eq. 1 accounts for the loss of particles of mass m due to their fragmentation into smaller particles (right side on Fig. 2), the function $b(m, m'; m'')$ being the distribution of outgoing fragments of mass m .

If $n_0(m) = n(m, 0)$, is the initial number density distribution per unit mass, then the total mass density, the total number density of grains and the mean mass of the initial distribution can be written as

$$M = \int_0^\infty m n_0(m) dm, \quad N_0 = \int_0^\infty n_0(m) dm, \quad m_0 = \frac{M}{N_0}. \quad (2)$$

The non-linear fragmentation equation writes in dimensionless form by using ([Kostoglou & Karabelas 2000](#))

$$\begin{cases} x \equiv m/m_0, \quad y \equiv m'/m_0, \quad \mathcal{K}(x, y) = K(m, m')/K(m_0, m_0), \\ \tau = (K(m_0, m_0)N_0)t, \quad f(x, \tau) = m_0 n(m, t)/N_0, \\ \tilde{b}(x, y; z) = m_0 b(m, m'; m''). \end{cases} \quad (3)$$

Here, $K(m_0, m_0)$ is a normalising constant with dimensions $[\text{length}]^3 [\text{time}]^{-1}$. We use the variables x , τ , and f for the dimensionless mass, time, and number density, respectively, to be consistent with the existing literature (e.g. [Kostoglou 2007](#); [Banasiak et al.](#)

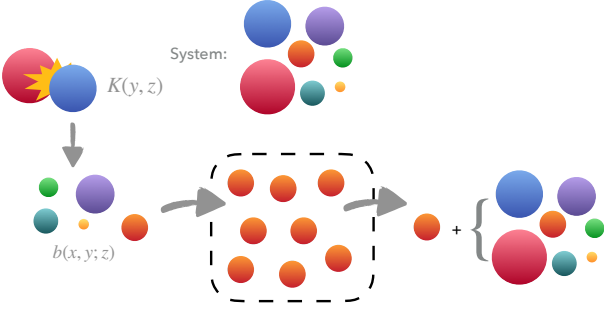


Figure 2. Scheme of the collisional fragmentation equation Eq. 1. The number density of orange grains, mass m increases due to fragmentation of the blue grains with mass greater than m , and decreases due to collision between an orange grain and any grain in the system.

2019) such that Eq. A1 writes

$$\begin{aligned} \frac{\partial f(x, \tau)}{\partial \tau} &= \int_0^\infty \int_x^\infty \mathcal{K}(y, z) \tilde{b}(x, y; z) f(y, \tau) f(z, \tau) dy dz \\ &\quad - f(x, \tau) \int_0^\infty \mathcal{K}(x, y) f(y, \tau) dy. \end{aligned} \quad (4)$$

Recently, Paul & Kumar (2018) have shown that Eq. 4 can be equivalently written in the conservative form

$$\begin{cases} \frac{\partial g(x, \tau)}{\partial \tau} - \frac{\partial F_{\text{frag}}[g](x, \tau)}{\partial x} = 0, \\ F_{\text{frag}}[g](x, \tau) \equiv \\ \int_0^\infty \int_x^\infty \int_0^x \frac{w}{wv} \tilde{b}(w, u; v) \mathcal{K}(u, v) g(v, \tau) g(u, \tau) dw du dv, \end{cases} \quad (5)$$

where $g(x, \tau) \equiv x f(x, \tau)$ is the mass density of grains per unit mass, and $F_{\text{frag}}[g](x, \tau)$ is the flux of mass density across the mass x triggered by fragmentation.

2.2 Kernels

The collision kernel is the same as the one used in coagulation theory (Hidy & Brock 1972; Kostoglou & Karabelas 2000; Ernst & Pagonabarraga 2007). The restriction on the form of \mathcal{K} is that it has to be a symmetric function, i.e. $\mathcal{K}(x, y) = \mathcal{K}(y, x)$. Exact solutions of the non-linear fragmentation equation are summarised in Table 1 for constant and multiplicative kernels. A constant kernel means that collision frequency is independent of the size of colliding grains. This is the case for an initial monodispersed system of grains for a short time period (Hidy & Brock 1972, and references therein). No physical interpretation can be given for the multiplicative kernel since, at least in the case of coagulation, it leads to a singularity in the Smoluchowski coagulation equation (Leyvraz & Tschudi 1981). In general, these simple kernels are only used to benchmark algorithms with their associated exact solution. The preferred fragmentation kernel used in astrophysics is the ballistic kernel described in Sect. 5.

2.3 Distribution of fragments

The function $\tilde{b}(x, y; z)$ is the probability density function for the formation of particle of mass x resulting from the break-up of particle of mass y due to its collision with a particle of mass z . The function $\tilde{b}(x, y; z)$ is an important physical quantity in the fragmentation process that determines the distribution of outgoing fragments of mass x (Cheng & Redner 1990; Kostoglou & Karabelas 2000; Banasiak et al. 2019). The z dependence in the function $\tilde{b}(x, y; z)$ reflects that a grain of mass y will give a different fragment distribution depending on the mass of the impactor. The function $\tilde{b}(x, y; z)$ satisfies the following requirements

$$\tilde{b}(x, y; z) = \begin{cases} \tilde{b}(x, y; z) & x, y, z > 0 \\ 0 & \forall x > y \end{cases} \quad (6)$$

and local conservation of mass

$$\forall y > 0, \int_0^y x \tilde{b}(x, y; z) dx = y, \quad (7)$$

such that the total mass of the fragments is equal to the mass of the parent particle y . According to Eq. 7, it is important to note that, after the collision, only particle y breaks up while z remains intact. According to the definition of \tilde{b} , the number of fragments writes

$$\tilde{N}(y; z) = \int_0^y \tilde{b}(x, y; z) dx. \quad (8)$$

Moreover, \tilde{b} should satisfy the following requirement (Kostoglou & Karabelas 2000; Banasiak et al. 2019)

$$\int_0^k x \tilde{b}(x, y; z) dx \geq \int_{y-k}^y (y-x) \tilde{b}(x, y; z) dx, \quad 0 \leq k \leq y/2. \quad (9)$$

The inequality in Eq. 9 ensures that when a fragment $x \geq y/2$ is formed, the mass from the remaining fragments between x and y (right-hand side) contributes to, but does not exceed, the total mass of grains between 0 and $k = y - x$ (left-hand side) that could additionally include some pre-existing (i.e. unbroken) grains. This ensures that no rearrangement of the mass is allowed.

2.4 Analytic solutions

The number density distribution that results from Eq. 4 is determined by the details of the collision kernel $\mathcal{K}(x, y)$ and the distribution of fragments $\tilde{b}(x, y; z)$. Exact solutions are known only for simple forms of \mathcal{K} (e.g. the constant and multiplicative kernels) and for homogeneous forms of \tilde{b} . Homogeneity implies that the distribution of fragments \tilde{b} can be written as a power law

$$\tilde{b}(x, y; z) = p(x/y)/y. \quad (10)$$

Due to the restrictions from Eqs. 7 and 9, p takes the form (McGrady & Ziff 1987; Cheng & Redner 1990; Ernst & Pagonabarraga 2007)

$$p(x) = (\beta + 2)x^\beta, \quad (11)$$

obeying,

$$\int_0^y x \tilde{b}(x, y; z) dx = y, \quad \tilde{N}(y) = \frac{\beta + 2}{\beta + 1}. \quad (12)$$

By definition, fragmentation results in at least two fragments. Therefore, the number of fragments satisfies $\tilde{N} \geq 2$ which implies

Kernel	$\mathcal{K}(x, y)$	exact solution
Constant	1	$f(x, \tau') = f(x, 0) \exp(-\tau') + \sqrt{2\tau'} \exp(-\tau') \int_x^\infty \frac{I_1(2\sqrt{2\tau' \log(y/x)}) f(y, 0)}{y \sqrt{\log(y/x)}} dy$
Multiplicative	xy	$f(x, \tau) = (1 + \tau)^2 \exp(-x(1 + \tau))$

Table 1. The two fragmentation kernels \mathcal{K} considered in this study with the corresponding exact solution.

$-1 < \beta \leq 0$. Exact solutions have been derived for the constant and multiplicative collision kernels in the case of binary breakage ($\beta = 0$) where $\tilde{b}(x, y; z) = 2/y$ (Ziff & McGrady 1985; Kostoglou & Karabelas 2000). Existence and uniqueness of the following exact solutions for the non-linear fragmentation equation have been proved recently (Paul & Kumar 2018; Barik & Giri 2018). We review these solutions (see Table 1) and they will be used to benchmark the algorithm in Sect. 4.

2.4.1 Constant kernel

By substituting $\mathcal{K}(x, y) = 1$ into Eq. 4, we obtain

$$\frac{\partial f(x, \tau)}{\partial \tau} = -Nf(x, \tau) + N \int_x^\infty \frac{p(x/y)}{y} f(y, \tau) dy, \quad (13)$$

where $N = \int_0^\infty f(x, \tau)$ is the dimensionless total number density of particles. By integrating Eq. 13 from $x = 0$ to $x = \infty$, the equation on N writes

$$\frac{dN}{d\tau} = (b_0 - 1)N^2 \Rightarrow N(\tau) = \frac{1}{1 - (b_0 - 1)\tau}, \quad (14)$$

where $b_0 = \int_0^1 p(w)dw$, with $w = x/y$. Details are given in Appendix B. An important remark is that there is a shattering phenomenon at $\tau_c = 1/(b_0 - 1)$ where the total number of particles diverges. The system no longer conserves mass as particles approach infinitely small masses, analogous to the gelation phenomenon for coagulation in the opposite limit (Ziff & McGrady 1985; Kostoglou & Karabelas 2000; Ernst & Pagonabarraga 2007). Then, by using the following change of variables for time

$$\tau' = \int_0^\tau N(t)dt = \frac{1}{1 - b_0} \log(1 - (b_0 - 1)\tau), \quad (15)$$

we obtain

$$\frac{\partial f(x, \tau')}{\partial \tau'} = -f(x, \tau') + \int_x^\infty \frac{1}{y} p(x/y) f(y, \tau') dy. \quad (16)$$

This is identical to the linear fragmentation equation with constant fragmentation rate (Ziff & McGrady 1985; Kostoglou & Karabelas 2000). The solution to Eq. 16 with a general initial condition and $p(x/y) = 2$ writes (Ziff & McGrady 1985)

$$f(x, \tau') = f(x, 0) \exp(-\tau') + \sqrt{2\tau'} \exp(-\tau') \int_x^\infty \frac{I_1(2\sqrt{2\tau' \log(y/x)}) f(y, 0)}{y \sqrt{\log(y/x)}} dy, \quad (17)$$

where I_1 is the modified Bessel function of first kind. For the benchmark of the numerical scheme in Sect. 4, the analytical solution is evaluated with the function `integrate` from the PYTHON library `scipy`.

2.4.2 Multiplicative kernel

The solution for the multiplicative kernel $\mathcal{K}(x, y) = xy$ and the initial condition $f_0(x, 0) = \exp(-x)$ has been derived by (Ziff &

McGrady 1985; Kostoglou & Karabelas 2000). Eq. 4 can be written as

$$\frac{\partial f(x, \tau)}{\partial \tau} = -xf(x, \tau) + 2 \int_x^\infty f(y, \tau) dy. \quad (18)$$

This is identical to the linear fragmentation equation with a linear fragmentation rate (Ziff & McGrady 1985; Kostoglou & Karabelas 2000). The solution of Eq. 18 writes

$$f(x, \tau) = (1 + \tau)^2 \exp(-x(1 + \tau)). \quad (19)$$

3 DISCONTINUOUS GALERKIN ALGORITHM

Lombart & Laibe (2021) showed that the discontinuous Galerkin (DG) method could be used to efficiently solve the Smoluchowski coagulation equation with a reduced number of mass bins. We now want to apply the same method to non-linear fragmentation described in Eq. 4. We refer the reader to Lombart & Laibe (2021) for a complete description of the general algorithm and here only detail the steps that are altered to model the non-linear fragmentation equation, i.e. the evaluation of the flux, the integral of the flux and the Courant-Friedrichs-Lewy condition (CFL). The algorithm flowchart is given in the github repository in Sect. 6.

3.1 Summary

Since the non-linear fragmentation Eq. 4 is defined over an unbounded mass interval $x \in \mathbb{R}_+$, the first step is to reduce the mass interval to a physically relevant mass range $[x_{\min} > 0, x_{\max} < +\infty]$, and divided into N bins. Each bin is defined by $I_j = [x_{j-1/2}, x_{j+1/2})$ for $j \in \llbracket 1, N \rrbracket$. The size and the center position of each bin are defined respectively by $h_j = x_{j+1/2} - x_{j-1/2}$ and $x_j = (x_{j+1/2} + x_{j-1/2})/2$. Eq. 5 is then multiplied by a Legendre polynomial basis function ϕ and integrated over each bin. After using an integral by part transformation, the DG method consist in solving the following equation

$$\int_{I_j} \frac{\partial g_j}{\partial x} \phi dx + \underbrace{\int_{I_j} F_{\text{frag}}[g](x, \tau) \frac{\partial \phi}{\partial x} dx}_{\text{integral of the flux see Sect. 3.3}} - F_{\text{frag}}[g](x_{j+1/2}, \tau) \phi(x_{j+1/2}) + F_{\text{frag}}(x_{j-1/2}, \tau) \phi(x_{j-1/2}) = 0, \quad (20)$$

where g_j is the Legendre polynomials approximation of g in bin I_j

$$\forall x \in I_j, g(x) \approx g_j(x, \tau) = \sum_{i=0}^k g_j^i(\tau) \phi_i(\xi_j(x)). \quad (21)$$

The function ξ map the bin interval into interval $[-1, 1]$ and k is the order of the Legendre polynomials.

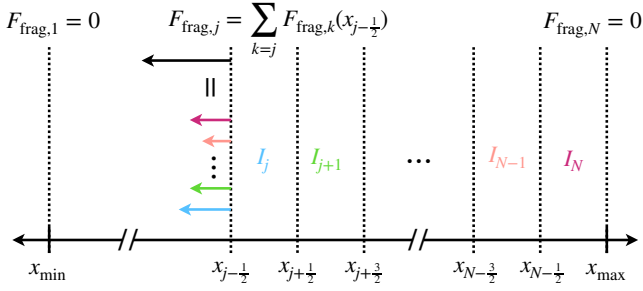


Figure 3. Illustration of the fragmentation flux of mass for bin j . $F_{\text{frag},j}$ can be seen as the cumulative contribution of sub-fluxes for each I_k transferring mass into the mass range $[x_{\text{xmin}}, x_{j-1/2}]$.

3.2 Numerical flux evaluation

The truncating fragmentation flux into the physically relevant mass range $[x_{\text{min}} > 0, x_{\text{max}} < +\infty]$ writes

$$F_{\text{frag}}[g](x, \tau) = \int_{x_{\text{min}}}^{x_{\text{max}}} \int_x^{x_{\text{max}}} \int_{x_{\text{min}}}^x \frac{w}{uv} \tilde{b}(w, u; v) \mathcal{K}(u, v) g(v, \tau) g(u, \tau) dw du dv. \quad (22)$$

Mass conservation is preserved by not allowing particles of mass larger than x_{max} or smaller than x_{min} to form.

3.2.1 Description of the flux

The fragmentation flux F_{frag} is non local, similar to the coagulation flux (Liu et al. 2019; Lombart & Laibe 2021), meaning that the evaluation of the flux at the interface $x_{j-1/2}$ depends on the evaluation of g_j in all bins. As a consequence, the fragmentation flux is a continuous function of mass across interfaces, i.e. $F_{\text{frag}}[g] = F_{\text{frag}}[g](x_{j-1/2}, \tau)$. This is in contrast to usual DG solvers in which the numerical flux is discontinuous and must be reconstructed at the interfaces (e.g Cockburn & Shu 1989; Zhang & Shu 2010).

Physically, $F_{\text{frag}}[g](x, \tau)$ represents the cumulative flux from all fragmentation processes which produce particles with mass lower than x from a particle that was greater than x , regardless of the bin in which they originated. In practice, since fragmentation tends to produce a mass flux towards smaller masses, we define the flux on the left edge of each bin (i.e. $F_{\text{frag},j} \equiv F_{\text{frag}}[g](x_{j-1/2})$, see Fig. 3). In Fig. 3, $F_{\text{frag},j}$ is equivalent to the sum of sub-fluxes defined as

$$\begin{aligned} \tilde{F}_{\text{frag},k} &\equiv \underbrace{\int_{I_k} \int_{x_{j-1/2}}^{x_{\text{max}}} \frac{\mathcal{K}(u, v)}{uv} g'_l(u, \tau) g_l(v, \tau)}_A \underbrace{\int_{x_{\text{min}}}^{x_{j-1/2}} w \tilde{b}(w, u; v) dw}_{B} du dv. \end{aligned} \quad (23)$$

Term B is the total mass density of particles in the range $[x_{\text{min}}, x_{j-1/2}]$ resulting from fragmentation of a particle $u \in [x_{j-1/2}, x_{\text{max}}]$. Term A accounts for the rate of fragmentation due to collisions between particles of mass u and a particle of mass $v \in I_k$. Therefore, each term $\tilde{F}_{\text{frag},k}$ transfers mass into $[x_{\text{min}}, x_{j-1/2}]$ and contributes to the flux $F_{\text{frag},j}$. The benefit of this convention is that we can ensure mass conservation by setting the outgoing and incoming flux to 0 at x_{min} and x_{max} , respectively. To avoid the prohibitive computational costs of approximating the flux numerically,

we take advantage of the polynomial expansion and calculate integrals analytically. For this method to work, both the collision kernel and the distribution of fragments have to be integrable functions, which is the case in this study. This approach maintains a high accuracy and a reasonable computational cost without multiplying the number of sampling points.

3.2.2 Procedure to evaluate the flux

The numerical flux is analytically integrated by using g_j , the approximation of g in the bin I_j (see Eq.14 in Lombart & Laibe 2021). We assume that the distribution of fragments and the collision kernel are explicitly integrable and separable as $\tilde{b}(w, u; v) = \tilde{b}_3(w) \tilde{b}_1(u) \tilde{b}_2(v)$ and $\mathcal{K}(u, v) = \mathcal{K}_1(u) \mathcal{K}_2(v)$, which is true for binary fragmentation when using the constant or multiplicative collision kernel:

$$\begin{cases} \tilde{b}(w, u; v) = \frac{2}{u} \Rightarrow \tilde{b}_3(w) \equiv 1, \tilde{b}_1(u) \equiv \frac{2}{u}, \tilde{b}_2(v) \equiv 1, \\ \mathcal{K}_{\text{const}}(u, v) = 1 \Rightarrow \mathcal{K}_1(u) \equiv 1, \mathcal{K}_2(v) \equiv 1, \\ \mathcal{K}_{\text{mul}}(u, v) = uv \Rightarrow \mathcal{K}_1(u) \equiv u, \mathcal{K}_2(v) \equiv v. \end{cases} \quad (24)$$

The scaled polynomials $p_j(x, \tau)$ replaces g_j to ensure positivity (Liu et al. 2019; Lombart & Laibe 2021)

$$\begin{aligned} p_j(x, \tau) &= \gamma_j (g_j(x, \tau) - \bar{g}_j) + \bar{g}_j, \\ \gamma_j &= \min \left\{ 1, \left| \frac{\bar{g}_j}{m_j - \bar{g}_j} \right| \right\}, \end{aligned} \quad (25)$$

where $m_j \equiv \min_{x \in I_j} g_j(x, \tau)$ and \bar{g}_j refers to the bin average of g_j in I_j

$$\bar{g}_j \equiv \frac{1}{h_j} \int_{I_j} g_j(x, \tau) dx = g_j^0(\tau) \quad (26)$$

Therefore, the numerical flux can be written as

$$\begin{aligned} F_{\text{frag}}(x_{j-1/2}, \tau) &= \sum_{l=1}^N \int_{I_l} \sum_{l'=j}^N \int_{I_{l'}} \sum_{q=1}^{j-1} \int_{I_q} \frac{w}{uv} \tilde{b}_3(w) \tilde{b}_1(u) \tilde{b}_2(v) \mathcal{K}_1(u) \mathcal{K}_2(v) p_{l'}(u, \tau) p_l(v, \tau) dw du dv, \\ &= \sum_{l=1}^N \sum_{l'=j}^N \sum_{q=1}^{j-1} \sum_{i'=0}^k \sum_{i=0}^k \gamma_l g_l^i(\tau) \gamma_{l'} g_{l'}^{i'}(\tau) T_{i',i}(j, l, l', i', i) T_w(j, q) \\ &+ \sum_{l=1}^N \sum_{l'=j}^N \sum_{q=1}^{j-1} \sum_{i'=0}^k (1 - \gamma_l) g_l^0(\tau) \gamma_{l'} g_{l'}^{i'}(\tau) T_{i',0}(j, l, l', i') T_w(j, q) \\ &+ \sum_{l=1}^N \sum_{l'=j}^N \sum_{q=1}^{j-1} \sum_{i=0}^k \gamma_l g_l^i(\tau) (1 - \gamma_{l'}) g_{l'}^0(\tau) T_{0,i}(j, l, l', i) T_w(j, q) \\ &+ \sum_{l=1}^N \sum_{l'=j}^N \sum_{q=1}^{j-1} (1 - \gamma_l) g_l^0(\tau) (1 - \gamma_{l'}) g_{l'}^0(\tau) T_{0,0}(j, l, l') T_w(j, q) \end{aligned} \quad (27)$$

where k is the order of polynomials p_j and

$$\begin{aligned}
T_{i',i}(j, l, l', i', i) &\equiv \\
&\int_{I_l} \int_{I_{l'}} \frac{\tilde{b}_1(u)}{u} \mathcal{K}_1(u) \phi_{i'}(\xi_{l'}(u)) \frac{\tilde{b}_2(v)}{v} \mathcal{K}_2(v) \phi_i(\xi_l(v)) dudv, \\
T_{i',0}(j, l, l', i') &\equiv \\
&\int_{I_l} \int_{I_{l'}} \frac{\tilde{b}_1(u)}{u} \mathcal{K}_1(u) \phi_{i'}(\xi_{l'}(u)) \frac{\tilde{b}_2(v)}{v} \mathcal{K}_2(v) dudv, \\
T_{0,i}(j, l, l', i) &\equiv \\
&\int_{I_l} \int_{I_{l'}} \frac{\tilde{b}_1(u)}{u} \mathcal{K}_1(u) \frac{\tilde{b}_2(v)}{v} \mathcal{K}_2(v) \phi_i(\xi_l(v)) dudv, \\
T_{0,0}(j, l, l') &\equiv \\
&\int_{I_l} \int_{I_{l'}} \frac{\tilde{b}_1(u)}{u} \mathcal{K}_1(u) \frac{\tilde{b}_2(v)}{v} \mathcal{K}_2(v) dudv, \\
T_w(j, q) &\equiv \int_{I_q} w \tilde{b}_3(w) dw.
\end{aligned} \tag{28}$$

Note that the terms $T_{i',i}$, $T_{i',0}$, $T_{0,i}$ and $T_{0,0}$ are calculated using the variables $\xi_{l'}$ and ξ_l for numerical stability, and that the negative sign for the fragmentation flux is taken into account in the operator \mathbf{L} (see Eqs. 16 and 27 in [Lombart & Laibe 2021](#)). All of the analytic formulae are derived and tested in MATHEMATICA before being translated to Fortran. The algorithm is written in Fortran and tested against the MATHEMATICA version for accuracy.

$T_{i',i}$, $T_{i',0}$, $T_{0,i}$ and T_w only need to be calculated once at the beginning of the scheme, since they are independent of time. In practice, we combine and store these values in arrays as follows. First we compute four arrays with element $T_{i',i}(j, l, l', i', i) T_w(j, q)$, $T_{i',0}(j, l, l', i') T_w(j, q)$, $T_{0,i}(j, l, l', i) T_w(j, q)$ and $T_{0,0}(j, l, l') T_w(j, q)$ such that when the subarrays for index j are multiplied respectively by $\gamma_l g_l^i(\tau) \gamma_{l'} g_{l'}^{i'}(\tau)$, $(1 - \gamma_l) g_l^0(\tau) \gamma_{l'} g_{l'}^{i'}(\tau)$, $\gamma_l g_l^i(\tau) (1 - \gamma_{l'}) g_{l'}^0(\tau)$, $(1 - \gamma_l) g_l^0(\tau) (1 - \gamma_{l'}) g_{l'}^0(\tau)$ and summed over all elements, we obtain the four term of the right-hand side of Eq. 27. Finally, the process is repeated for all j to obtain F_{frag} .

3.3 Integral of the flux

By defining $\mathcal{F}_{\text{frag}}$ as the integral of the numerical flux Eq. 20 and (see Eq.12 in [Lombart & Laibe 2021](#)), then together with Eq. 22 we obtain

$$\begin{aligned}
\mathcal{F}_{\text{frag}}(j, k', \tau) &= \\
&\int_{I_j} \int_{x_{\min}}^{x_{\max}} \int_x^{x_{\max}} \int_{x_{\min}}^x \frac{w}{uw} \tilde{b}(w, u; v) \mathcal{K}(u, v) g(v, \tau) g(u, \tau) \\
&\quad \times \partial_x \phi_{k'}(\xi_j(x)) dw dudv dx,
\end{aligned} \tag{29}$$

where $k' \in [0, k]$. By splitting the integral over v into two integrals, one for $u \in [x, x_{j+1/2}]$ and the second for $u \in [x_{j+1/2}, x_{\max}]$, and

by approximating g with the scale polynomials p , we obtain

$$\begin{aligned}
\mathcal{F}_{\text{frag}}(j, k', \tau) &= \\
&= \sum_{l=0}^N \sum_{i'=0}^k \sum_{i=0}^k \gamma_j g_j^{i'}(\tau) \gamma_{l'} g_{l'}^i(\tau) \mathcal{T}_{w,u,i'}^1(j, k, i', x_{\min}) \mathcal{T}_{v,i}(j, l, i) \\
&+ \sum_{l=0}^N \sum_{i'=0}^k \gamma_j g_j^{i'}(\tau) (1 - \gamma_l) g_l^0(\tau) \mathcal{T}_{w,u,i'}^1(j, k, i', x_{\min}) \mathcal{T}_{v,0}(j, l, i) \\
&+ \sum_{l=0}^N \sum_{i=0}^k (1 - \gamma_j) g_j^0(\tau) \gamma_{l'} g_{l'}^i(\tau) \mathcal{T}_{w,u,0}^1(j, k, x_{\min}) \mathcal{T}_{v,i}(j, l, i) \\
&+ \sum_{l=0}^N (1 - \gamma_j) g_j^0(\tau) (1 - \gamma_{l'}) g_{l'}^0(\tau) \mathcal{T}_{w,u,0}^1(j, k, x_{\min}) \mathcal{T}_{v,0}(j, l, i) \\
&+ \sum_{l=0}^N \sum_{l'=j+1}^N \sum_{i'=0}^k \sum_{i=0}^k \gamma_{l'} g_{l'}^{i'}(\tau) \gamma_l g_l^i(\tau) \\
&\quad \times \mathcal{T}_{w,u,i'}^2(j, k, l', i', x_{\min}) \mathcal{T}_{v,i}(j, l, i) \\
&+ \sum_{l=0}^N \sum_{l'=j+1}^N \sum_{i'=0}^k \gamma_{l'} g_{l'}^{i'}(\tau) (1 - \gamma_l) g_l^0(\tau) \\
&\quad \times \mathcal{T}_{w,u,i'}^2(j, k, l', i', x_{\min}) \mathcal{T}_{v,0}(j, l, i) \\
&+ \sum_{l=0}^N \sum_{l'=j+1}^N \sum_{i=0}^k (1 - \gamma_{l'}) g_{l'}^0(\tau) \gamma_l g_l^i(\tau) \\
&\quad \times \mathcal{T}_{w,u,0}^2(j, k, l', x_{\min}) \mathcal{T}_{v,i}(j, l, i) \\
&+ \sum_{l=0}^N \sum_{l'=j+1}^N (1 - \gamma_{l'}) g_{l'}^0(\tau) (1 - \gamma_l) g_l^0(\tau) \\
&\quad \times \mathcal{T}_{w,u,0}^2(j, k, l', x_{\min}) \mathcal{T}_{v,0}(j, l, i),
\end{aligned} \tag{30}$$

where

$$\begin{aligned}
\mathcal{T}_{w,u,i'}^1(j, k, i', x_{\min}) &\equiv \\
&\int_{I_j} \int_{x_{\min}}^x \int_x^{x_{j+1/2}} w \tilde{b}_3(w) \frac{\tilde{b}_1(u)}{u} \mathcal{K}_1(u) \phi_{i'}(\xi_j(u)) \\
&\quad \times \partial_x \phi_{k'}(\xi_j(x)) dudw dx, \\
\mathcal{T}_{w,u,0}^1(j, k, x_{\min}) &\equiv \\
&\int_{I_j} \int_{x_{\min}}^x \int_x^{x_{j+1/2}} w \tilde{b}_3(w) \frac{\tilde{b}_1(u)}{u} \mathcal{K}_1(u) \partial_x \phi_{k'}(\xi_j(x)) dudw dx, \\
\mathcal{T}_{w,u,i'}^2(j, k, l', i', x_{\min}) &\equiv \\
&\int_{I_j} \int_{x_{\min}}^x \int_{I_{l'}} \frac{\tilde{b}_1(u)}{u} \mathcal{K}_1(u) \phi_{i'}(\xi_{l'}(u)) \\
&\quad \times \partial_x \phi_{k'}(\xi_j(x)) dudw dx,
\end{aligned} \tag{31}$$

$$\begin{aligned}
\mathcal{T}_{w,u,0}^2(j, k, l', x_{\min}) &\equiv \\
&\int_{I_j} \int_{x_{\min}}^x \int_{I_{l'}} w \tilde{b}_3(w) \frac{\tilde{b}_1(u)}{u} \mathcal{K}_1(u) \partial_x \phi_{k'}(\xi_j(x)) dudw dx,
\end{aligned}$$

$$\mathcal{T}_{v,i}(j, l, i) \equiv \int_{I_l} \frac{\tilde{b}_2(v)}{v} \mathcal{K}_2(v) \phi_i(\xi_l(v)) dv,$$

$$\mathcal{T}_{v,0}(j, l) \equiv \int_{I_l} \frac{\tilde{b}_2(v)}{v} \mathcal{K}_2(v) dv.$$

Table 2. CFL condition for linear and quadratic fragmentation rates.

Type	$\mathcal{K}(x, y)$	$\Delta\tau_{\text{CFL}}$
constant	1	2.8
multiplicative	xy	4.0×10^{-3}

This allows $\mathcal{F}_{\text{frag}}$ to be evaluated similarly to the numerical flux in Eq. 27. After a change of variables into ξ_l and ξ_j , triple integrals are derived with MATHEMATICA and translated into FORTRAN. Similar to the arrays in Eq. 28, $\mathcal{T}_{w,u,i'}^1$, $\mathcal{T}_{w,u,0}^1$, $\mathcal{T}_{w,u,i'}^2$, $\mathcal{T}_{w,u,0}^2$, $\mathcal{T}_{v,i}$ and $\mathcal{T}_{v,0}$ need only to be computed once at the beginning of the scheme. Then, $\mathcal{F}_{\text{frag}}$ is reduced to the sum of four terms in Eq. 30. The first term is obtained by computing the product of the subarray of $\mathcal{T}_{w,u,i'}^1(j, k, i', x_{\min})\mathcal{T}_{v,i}(j, l, i)$ with $\gamma_j g_j^{i'}(\tau)\gamma_l g_l^i(\tau)$ and summing over all elements. The same process is applied for the other terms. Importantly, accuracy depends only on the order of polynomials to approximate g , since the integral terms in F_{frag} and $\mathcal{F}_{\text{frag}}$ are evaluated analytically.

3.4 CFL condition

Analytic solutions shown in Sect. 2.4 are of the same form as the linear fragmentation equation (Kostoglou & Karabelas 2000; Kumar et al. 2014; Liu et al. 2019). Therefore, the CFL condition (CFL) is determined by using the conservative form of the linear fragmentation equation with the flux F_{linfrag} . The DG scheme for order 0 applied to the linear fragmentation equation corresponds to the forward Euler discretisation, i.e.

$$g_j^{0,n+1} = g_j^{0,n} - \frac{\Delta\tau}{\Delta x_j} [F_{\text{linfrag}}(x_{j+1/2}, \tau) - F_{\text{linfrag}}(x_{j-1/2}, \tau)], \quad (32)$$

for the n -th time step. The stability condition of the scheme is determined by the CFL condition, which is evaluated to ensure the positivity of the bin average $g_j^{0,n+1} = \bar{g}_j^{n+1} > 0$ at time-step $n+1$ (Filbet & Laurecot 2004; Kumar 2007; Lombart & Laibe 2021), i.e.

$$g_j^{0,n+1} > 0 \Rightarrow \Delta\tau \sup_j \left(\frac{1}{\Delta x_j} \int_{I_j} \frac{a(v)}{v} dv \int_{x_{\min}}^{x_{j-1/2}} ub(u, x_j) du \right) < 1, \quad (33)$$

where $b(u, x_j) = 2/x_j$, $a(v) = v$ for the multiplicative kernel and $a(v) = 1$ for the constant kernel. Details of the derivation are given in Appendix C. Unfortunately, we did not succeed in obtaining a better CFL criterion with the method based on the Laplace transform presented in Laibe & Lombart (2022). Table 2 gives the CFL condition for the constant and multiplicative kernels. For the constant collision kernel case, it is required to apply the change of time variable detailed in Eq. 15. The DG method writes

$$\frac{dg_j(\tau')}{d\tau'} = \exp(-\tau') \mathbf{L}[g], \quad (34)$$

where \mathbf{g} and \mathbf{L} are defined in Eqs. 14 and 16 in Lombart & Laibe (2021). Therefore, the time step changes into

$$\Delta\tau' \rightarrow \exp(-\tau'_n) \Delta\tau'. \quad (35)$$

In practice, we use the same CFL than the multiplicative kernel to reduce numerical errors.

4 NUMERICAL RESULTS

The numerical scheme presented in Sect. 3 is tested against the exact solutions detailed in Sect. 2.4. Tests are performed with a limited number of bin, $N = 20$, consistent with constrains from 3D hydrodynamical simulations. The algorithm flowchart in detail is given in the github repository in Sect. 6.

4.1 Evaluation of errors

The strategy for error measurements is similar to Lombart & Laibe (2021). The experimental order of convergence (EOC, Liu et al. 2019) and the efficiency of the algorithm are analysed. The continuous and discrete L^1 norm writes

$$e_{c,N}(\tau) \equiv \sum_{j=1}^N \frac{h_j}{2} \sum_{\alpha=1}^R \omega_\alpha |g_j(x_j^\alpha, \tau) - g(x_j^\alpha, \tau)|, \quad (36)$$

$$e_{d,N}(\tau) \equiv \sum_{j=1}^N h_j |g_j(\hat{x}_j, \tau) - g(\hat{x}_j, \tau)|,$$

where g and g_j are the analytic and the numerical solutions of the linear fragmentation equation, $R = 16$ is the number of points used for the gaussian quadrature method, and $\hat{x}_j \equiv \sqrt{x_{j-1/2}x_{j+1/2}}$ is the geometric mean of bin I_j .

The EOC is defined as

$$\text{EOC} \equiv \frac{\ln\left(\frac{e_N(\tau)}{e_{2N}(\tau)}\right)}{\ln(2)}, \quad (37)$$

where e_N is the error evaluated for N cells and e_{2N} for $2N$ cells. For the calculation of the EOC, the numerical errors are calculated after one time-step at time $\tau = 10^{-3}$ for constant and multiplicative kernels in order to avoid time stepping errors. The total mass density of the system, the first moment of $g(x, \tau)$, writes

$$M_{1,N}(\tau) \equiv \int_{x_{\min}}^{x_{\max}} g(x, \tau) dx = \sum_{j=1}^N h_j g_j^0(\tau). \quad (38)$$

The absolute error of the total mass density is given by

$$e_{M_{1,N}}(\tau) \equiv \frac{|M_{1,N}(\tau) - M_1|}{M_1}, \quad (39)$$

where M_1 is the first moment of order of g for the exact solution and is constant in time. Here, we compare only absolute gains in order to interface the algorithm with hydrodynamical solvers.

4.2 Implementation details

Numerical solutions for the constant and multiplicative kernels are benchmarked against the exact solutions given in Eqs. 17 and 19. Simulations are performed for a mass interval $x \in [10^{-6}, 10^3]$. Tests are performed with FORTRAN in double precision and errors are calculated with PYTHON. Numerical solutions are shown only for polynomials of order $k = 0, 1, 2, 3$. For $k > 3$, arithmetics of large numbers generate non negligible errors. The initial condition (see Eq.17 in Lombart & Laibe 2021) is evaluated by a Gauss-Legendre quadrature method with five points to satisfy the analytical solution at time $\tau = 0$, with the majority of the mass contained in large grains. After a finite time τ , fragmentation has redistributed the mass to smaller grain sizes and we can compare the analytical and numerical solutions for accuracy. Simulations are performed with

constant time steps of $\Delta\tau_{\text{in}} = 10^{-3}$ for constant and multiplicative kernels to satisfy the respective CFL conditions (see Table 2). Simulations are performed sequentially on an Intel Core i7 2.8GHz. We use the `gfortran v11.2.0` compiler.

4.3 Multiplicative kernel

4.3.1 Conservation of mass and positivity of numerical solutions

Numerical solutions with orders of polynomials varying from $k = 0$ to $k = 3$ for $N = 20$ bins are benchmarked against analytical solutions at $\tau = 500$, in Fig. 4. The numerical solutions are positive due to the combination of the slope limiter and the Strong Stability Preserving Runge-Kutta (SSPRK) time stepping (see Sect. 3.4 and Sect. 3.5 in Lombart & Laibe 2021). Fig. 5.(a) shows the absolute error $e_{M_1, N}$ for $N = 20$ bins from $\tau = 10^{-3}$ to $\tau = 500$. As expected, the mass is conserved for all orders k .

4.3.2 Accuracy of the numerical solution

The accuracy of the numerical solutions improves with order of the polynomials. Fig. 5.(b) shows the numerical solution obtained at $\tau = 500$ in log-log scale. The numerical diffusion is drastically reduced (by up to a factor 1000) in the exponential tail as the order of the scheme increases. The major part of the total mass is localised around the maximum of the curve. The zoomed-in panel shows a linear scaling of this region, where it is evident that numerical solutions with order $k = 1, 2, 3$ achieve absolute errors of order $\sim 0.1 - 1\%$ while errors of order $\sim 20\%$ are obtained with $k = 0$.

4.3.3 Convergence of the numerical scheme

Figs. 5.(c),(d) show the numerical errors introduced in Sect. 4.1 at $\tau = 10^{-3}$. We use $e_{c, N}$ and $e_{d, N}$ from order 0 to order 3 as a function of the number of bins per decade $N_{\text{bin/dec}}$ to determine the EOC independently from the mass range. On the left, the EOC for the continuous L^1 norm is of order $k + 1$. On the right, the EOC for the discrete L^1 norm is of order $k + 2$ for odd polynomials, and $k + 1$ for even polynomials. From $e_{d, N}$, the expected accuracy of order $\sim 0.1\%$ is achieved with more than 10 bins/decade with $k = 0, 1, \sim 6$ bins/decade with $k = 2$ and ~ 4 bins/decade with $k = 3$. Errors of order $\sim 1\%$ is reached with ~ 10 bins/decade for $k = 0, 1$, with ~ 3 bins/decade for $k = 2$, and with ~ 2 bins/decade for $k = 3$.

4.3.4 Stability of the numerical scheme

Figs. 5.(e),(f) show the time evolution for $e_{c, N}$ and $e_{d, N}$. Despite only using $N = 20$ bins, both the continuous and discrete errors for each order remain bounded over the entire time interval (albeit with different accuracy).

4.4 Constant kernel

For constant case, the analytic solution Eq. 17 is evaluated for 1000 points logarithmically spaced with the function `integrate` in library `scipy`. Figures 6 and 7 show the test results for the constant kernel (comparable to Figs.4 and 5). Numerical solutions preserve

	$k = 0$	$k = 1$	$k = 2$	$k = 3$
time (s)	9.10^{-4}	2.10^{-2}	5.10^{-2}	9.10^{-2}

Table 3. Elapsed wall time in second for a single time-step for each orders when using constant or multiplicative kernel.

positivity and errors have similar magnitude compares to the multiplicative case after the same number of time steps.

5 DISCUSSION

The high-order numerical scheme based on the Discontinuous Galerkin method presented in Sect. 3 requires arithmetic of large numbers for polynomials of high-order. Thus, in its current form, order $k = 3$ is the maximum limit of the algorithm. Table 3 gives the elapsed wall time for a single time-step for each order when using the constant or multiplicative kernel. Using the code `PHANTOM` (Price et al. 2018) with a typical multifluid simulation with 10 dust sizes embedded in a protoplanetary disc with 10^6 SPH particles and 32 cpu, one hydrodynamical time-step takes ~ 1 s. The CFL condition detailed in Sect.3.4 for fragmentation will likely impose a sub-cycling of the hydrodynamic time-step, potentially creating a computational bottleneck. To avoid this bottleneck, two strategies may help to reach a one-to-one ratio: i) using a specific change of variable to reduce the number of time-steps (Carrillo & Goudon 2004; Goudon et al. 2013), and ii) using GPU parallelisation, since the fragmentation solver can be used independently for each SPH particle, which is highly parallelisable. Moreover, implicit time-stepping can be implemented in a manageable way because the number of dust bins has been kept minimal. We will be testing these strategies to further gain accuracy and computation efficiency in the future.

The collisional fragmentation model presented in this study considers that only one of the two colliding particles breaks up. No rearrangement of mass is allowed, i.e. mass transfer during the fragmentation process is not taken into account (Kostoglou & Karabelas 2000; Banasiak et al. 2019). Actually, the form of Eq. 4 implicitly assumes the mass of fragments in a collision does not exceed the mass of the parent particle y (see Eq. 12 and surrounding text). However, experiments have shown that some fragmentation events do lead to mass transfer between colliding grains, including cases where one of the colliders ends up with more mass than it started (Bukhari Syed et al. 2017; Blum 2018). To account for this more general case, we could consider the impact as a two-step process. The first step is the same as before with only one of the impacting grains fragmenting. The second step occurs immediately afterwards with one of the fragments sticking to the unbroken grain, leading to an increase in mass. While the latter is technically a coagulation process, it differs from the typical events modelled in the coagulation equation because interactions with the unbroken grain are limited to the distribution of fragments of the broken grain (as opposed to the entire grain size distribution). In such a scenario, Eq. 4 has to be modified as follows (Banasiak et al. 2019)

$$\frac{\partial f(x, \tau)}{\partial \tau} = \frac{1}{2} \int_0^\infty \int_0^\infty \mathcal{K}(y, z) \bar{b}(x, y; z) f(y, \tau) f(z, \tau) dy dz - f(x, \tau) \int_0^\infty \mathcal{K}(x, y) f(y, \tau) dy, \quad (40)$$

where $\bar{b}(x, y; z)$ is the distribution of fragments and a symmetric

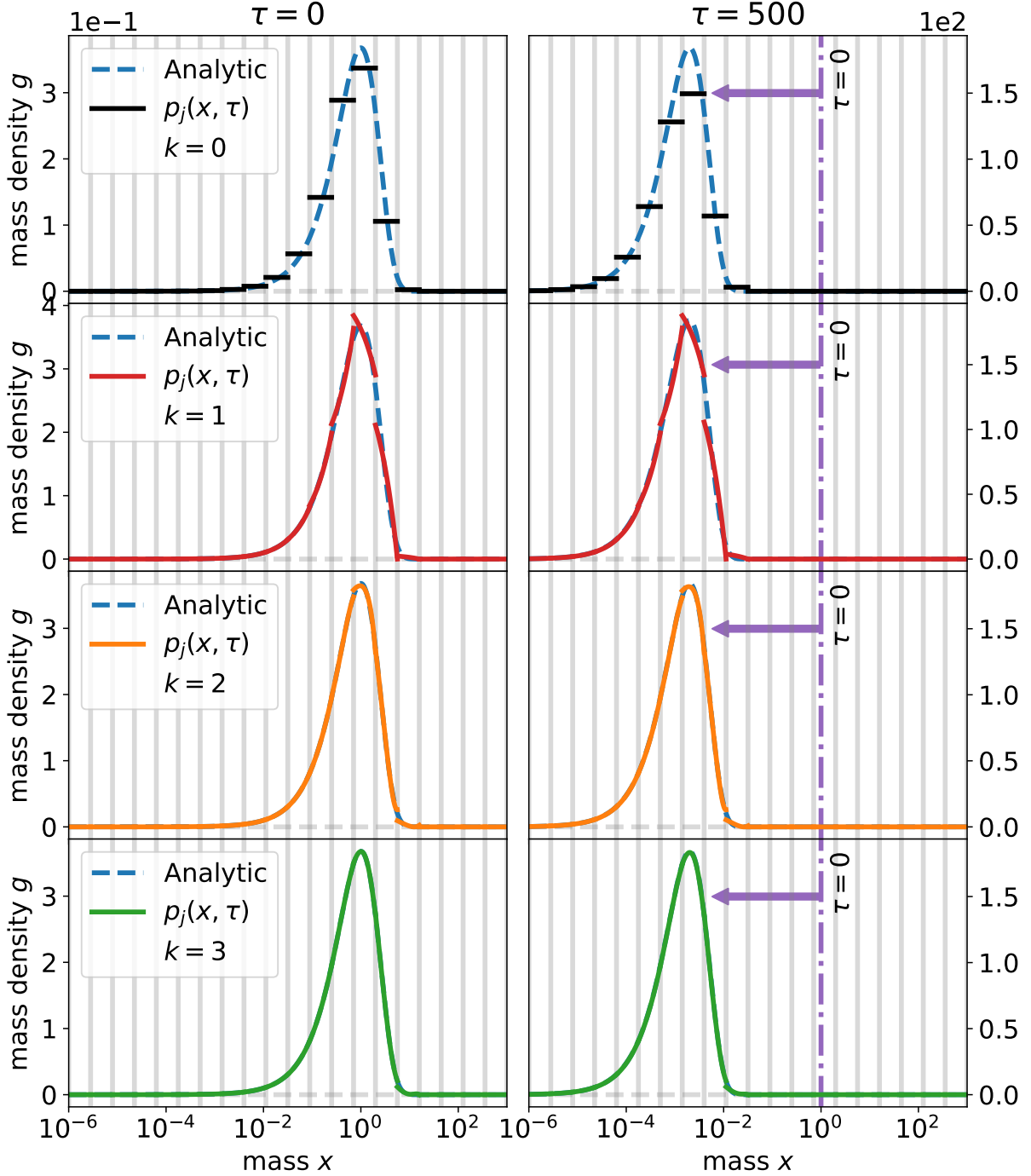


Figure 4. Test for the multiplicative kernel. Solid lines show the numerical solution $p_j(x, \tau)$ for $N = 20$ bins and $k = 0, 1, 2, 3$ at time $\tau = 0$ (left) and $\tau = 500$ (right). The exact solution $g(x, \tau)$ is given by the blue dashed line. Vertical grey lines represent the boundaries of the bins while the purple dashed lines in the panels on the right indicate the peak of the initial distribution to highlight the evolution due to fragmentation indicated by the purple arrow (note the nearly three orders of magnitude difference between the left and right vertical axes). The accuracy improves for larger values of k . Order 3 recovers the peak of the mass distribution with an accuracy of order $\sim 0.1\%$.

function in y and z . The symmetric property of function \mathcal{K} and $\bar{b}(x, y; z)$ explains the factor $1/2$ (i.e. collisions are counted twice in the integral). The new criterion for mass conservation is

$$\int_0^{y+z} x \bar{b}(x, y; z) dx = y + z, \quad \forall x > y + z, \quad \bar{b}(x, y; z) = 0. \quad (41)$$

Eq. 4 can be recovered from Eq. 40 by considering the symmetric property of the distribution of fragments (Banasiak et al. 2019)

$$\bar{b}(x, y, ; z) = \tilde{b}(x, y; z)H(y - x) + \tilde{b}(x, z; y)H(z - x), \quad (42)$$

where H is the Heaviside function. In future work, the DG scheme will be applied to the general non-linear fragmentation equation Eq. 40 in its conservative form.

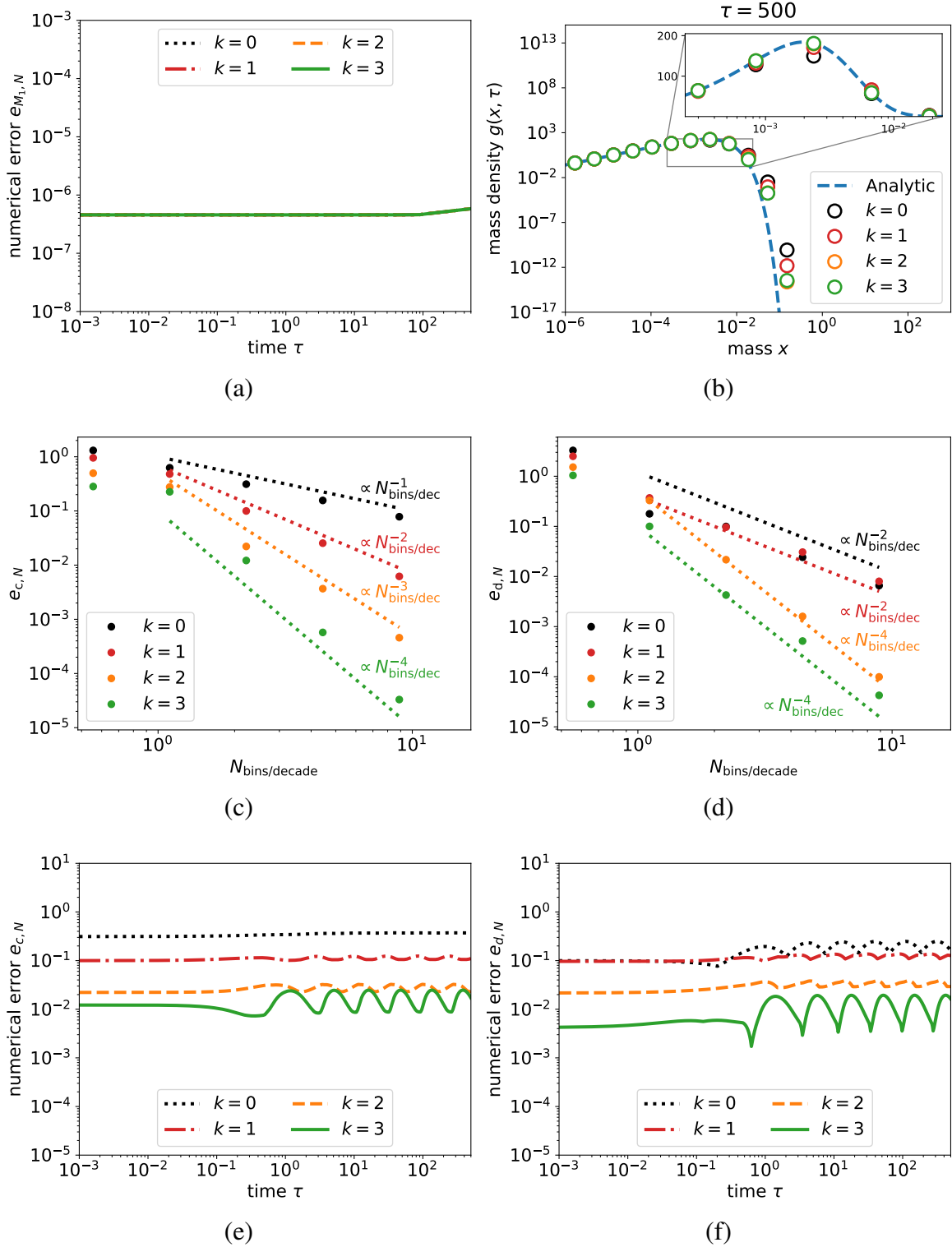


Figure 5. Test for the multiplicative kernel with $N = 20$ bins. Fig. (a): evolution of the absolute error $e_{M_1, N}$ on the moment $M_{1, N}$ for $N = 20$ bins. The mass is conserved. Fig. (b): numerical solution $p_j(x, \tau)$ evaluated with the geometric mean \hat{x}_j over each bin I_j . A zoom-in of the peak of the distribution shows that an absolute error of $\sim 0.1 - 1\%$ is reached with $k = 1, 2, 3$, compared to 20% obtained with $k = 0$. Accuracy in the exponential tail is improved by a factor 1000 with $k = 3$ compared to $k = 0$. Figs. (c),(d): the continuous L^1 error $e_{c, N}$ and the discrete L^1 error $e_{d, N}$ are plotted versus the number of bins per decade. The experimental order of convergence is $\text{EOC} = k + 1$ for $e_{c, N}$ and for $e_{d, N}$ $\text{EOC} = k + 1$ for polynomials of odd orders and $\text{EOC} = k + 2$ for polynomials of even orders. An accuracy of 0.1% is achieved with more than 10 bins/decade for $k = 0, 1$, with ~ 6 bins/decade for $k = 2$ and with ~ 4 bins/decade for $k = 3$. An accuracy of 1% is achieved with ~ 10 bins/decade for $k = 0, 1$, with ~ 3 bins/decade for $k = 2$ and ~ 2 bins/decade for $k = 3$. Figs. (e),(f): time evolution of the L^1 continuous and discrete norms, showing they remain bounded at large times.

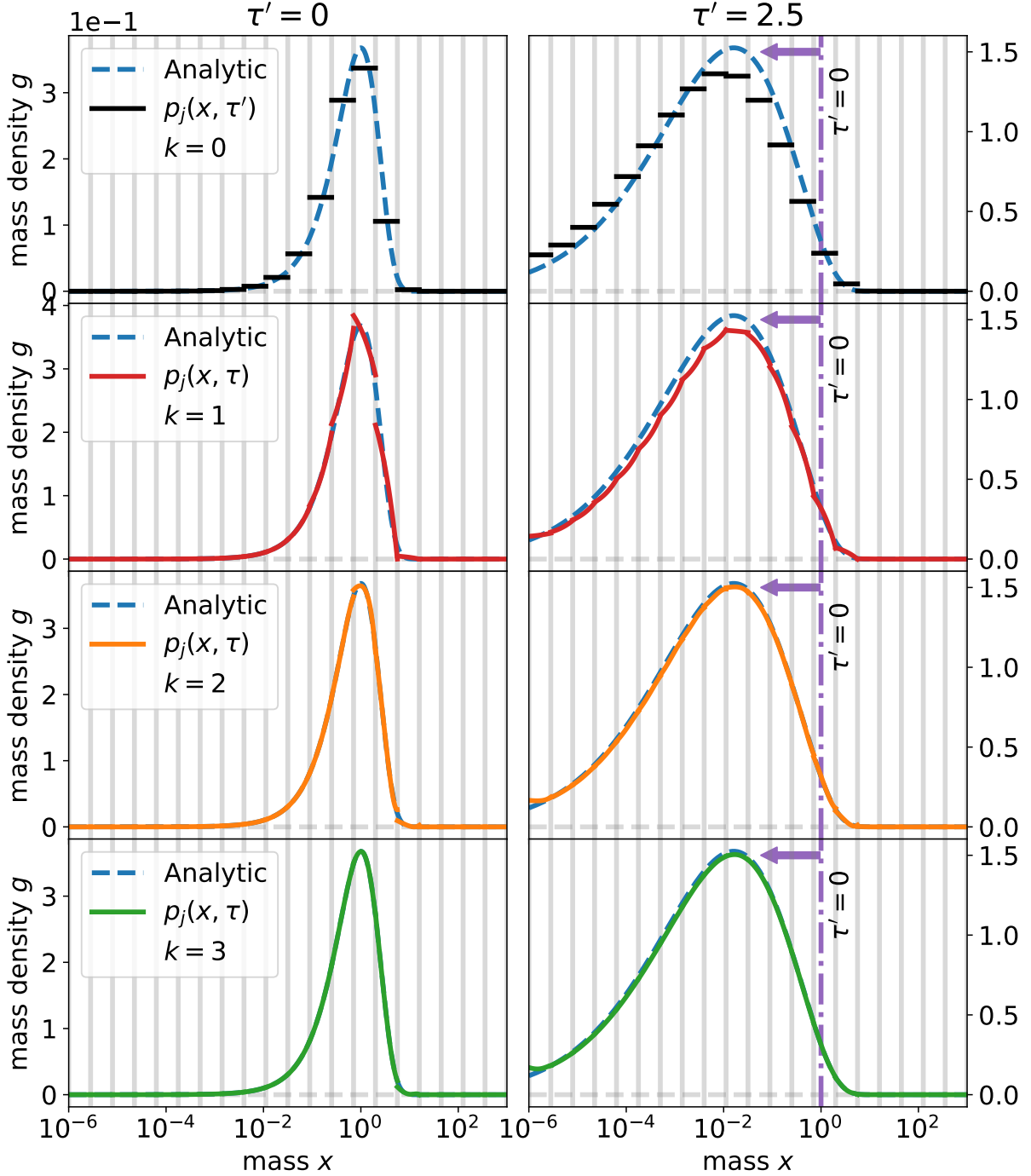


Figure 6. As in Fig. 4, but using the constant kernel from $\tau' = 0$ to $\tau' = 2.5$.

Physically, the fragmentation kernel used in astrophysics is the ballistic kernel defined as

$$K(x, y) \equiv (1 - \beta(x, y, \Delta v)) \Delta v(x, y) \sigma(x, y), \quad (43)$$

where Δv is the mean relative velocity between two grains of masses x and y , σ is the mean effective cross section of collision and β denotes the mean sticking probability of the grains. In this study, where only fragmentation is considered, then $\beta = 0$. The microphysics of collisions are encoded inside σ and Δv , those parameters depending *a priori* on the sizes of the colliding grains or the kinetic and thermo-

dynamical parameters of the surrounding medium. If we assume the grains are not charged, then we can ignore the complicating effects of electrostatic forces and σ reduces to the sum of the radii of the colliding dust grains. Unfortunately, even with these simplifications, the ballistic kernel does not yield analytic solutions and numerical solutions are required. Future developments will be to implement the ballistic kernel in the general non-linear fragmentation model (Eq. 40).

By nature, fragmentation and coagulation are stochastic processes, but random fluctuations in the solution can not be computed with

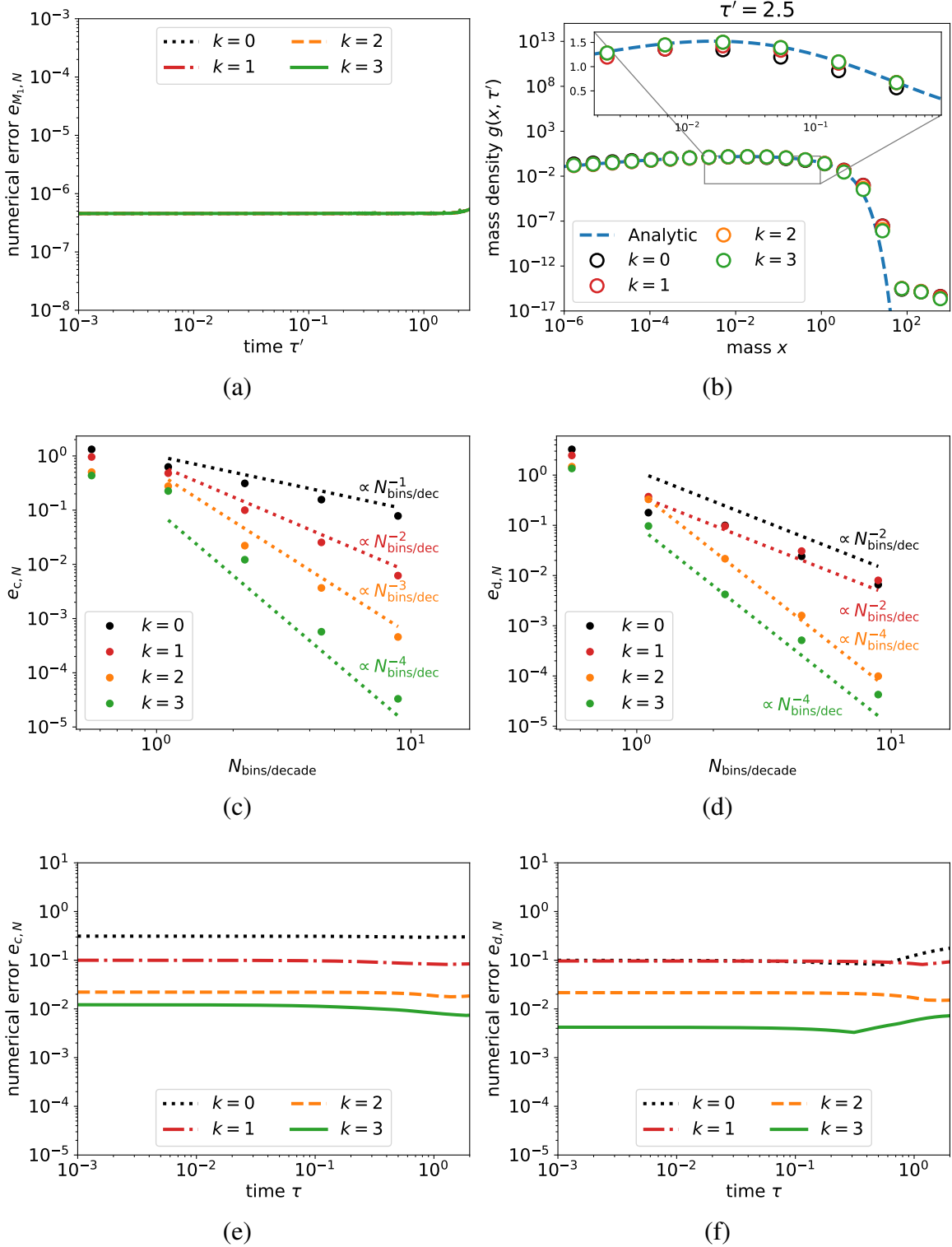


Figure 7. As in Fig. 5 but using the constant kernel.

Eq. 4. Given that such fluctuations cannot be constrained by current observations, this is not a critical limitation of the model. More importantly, there is nothing in the scheme that would prevent stochasticity from being added to the model. Additional physical processes, such as fragmentation of aggregates, can be implemented in the

solver by extending Eq. 4. In this case, the collision kernel \mathcal{K} has to be rewritten to include the adapted cross-section (Friedlander et al. 2000)

$$\mathcal{K}(x, y) \sim (x^{1/D_f} + y^{1/D_f}) \Delta v(x, y), \quad (44)$$

where D_f is the fractal dimension calculated by the collision al-

gorithm, such as Particle-Cluster Aggregation (PCA) or Cluster-Cluster Aggregation (CCA) (Dominik & Tielens 1997; Paszun & Dominik 2009; Dominik et al. 2016).

6 CONCLUSION

Fragmentation resulting from colliding grains is an important process that helps to regulate the smaller end of the evolving dust size distribution. Chemical, thermal and dynamical processes strongly depend on the dust size distribution, highlighting the need for accurate dust models that include coagulation and fragmentation. We have presented a high-order DG algorithm that accurately solves the non-linear fragmentation equation on a reduced mass grid of ~ 20 bins in order to provide an efficient algorithm that can feasibly couple with 3D hydrodynamic codes. Importantly, the DG scheme meets all of the physical and numerical requirements to accomplish this goal, including: i) a strictly positive mass density maintained over the entire numerical grid made possible by a strong stability preserving Runge Kutta time solver combined with a slope limiter, ii) conservation of mass at machine precision, iii) accuracy of order 0.1 – 1% is reached by high-order discretisation in time and mass space and iv) a fast algorithm with manageable time and memory costs due to analytically computed integrals and the ability to run with a limited number of bins.

The non-linear fragmentation model presented in this study describes the fragmentation of only one of the two colliding grains. The most general case consists of fragmentation and potential mass transfer between two colliding aggregates of arbitrary size. Although this model has been widely used in astrophysics (Safronov 1972; Tanaka et al. 1996; Birnstiel et al. 2010; Hirashita et al. 2021), numerical algorithms have never been compared to exact solutions, which to our knowledge have only been derived recently (Banasiak et al. 2019). Another crucial ingredient affecting the mass flux in physical models is coagulation. The methods we have developed in Paper I and Paper II (this study) are compatible with those developed earlier by Lombart & Laibe (2021) for coagulation. We will combine these processes in a future study and test their performance on real astrophysical mixtures.

ACKNOWLEDGEMENTS

This work has received funding from the Ministry of Science and Technology, Taiwan (MOST 110-2636-M-003-001). ML acknowledges funding from the ERC CoG project PODCAST No 864965. This project has received funding from the European Union’s Horizon 2020 research and innovation programme under the Marie Skłodowska-Curie grant agreement No 823823. MAH acknowledges support from the Excellence Cluster ORIGINS, which is funded by the Deutsche Forschungsgemeinschaft (DFG, German Research Foundation) under Germany Excellence Strategy - EXC-2094 - 390783311 and partial funding by the Deutsche Forschungsgemeinschaft (DFG, German Research Foundation) - 325594231. We used MATHEMATICA (Wolfram Research 14). We thank the anonymous referee for useful comments and discussions.

DATA AVAILABILITY

The data and supplementary material underlying this article are available in the repository "nonlinear_frag" on GitHub at https://github.com/mlombart/nonlinear_frag.git. Figures can be reproduced following the file README.md. The repository contains data and Python scripts used to generate figures.

REFERENCES

- Andrews S. M., 2020, *ARA&A*, **58**, 483
- Austin L., 1971, *Powder Technology*, **5**, 1
- Banasiak J., Lamb W., Laurençot P., 2019, Analytic Methods for Coagulation-Fragmentation Models, Volume I. Chapman and Hall/CRC, doi:10.1201/9781315154428
- Barik P. K., Giri A. K., 2018, arXiv e-prints, p. arXiv:1802.07969
- Birnstiel T., Dullemond C. P., Brauer F., 2010, *A&A*, **513**, A79
- Birnstiel T., Fang M., Johansen A., 2016, *Space Sci. Rev.*, **205**, 41
- Blum J., 2018, *Space Sci. Rev.*, **214**, 52
- Botte W. F., Durda D. D., Nesvorný D., Jedicke R., Morbidelli A., Vokrouhlický D., Levison H., 2005, *Icarus*, **175**, 111
- Brauer F., Dullemond C. P., Henning T., 2008, *A&A*, **480**, 859
- Brilliantov N., Krapivsky P. L., Bodrova A., Spahn F., Hayakawa H., Stadnichuk V., Schmidt J., 2015, *Proceedings of the National Academy of Science*, **112**, 9536
- Bukhari Syed M., Blum J., Wahlberg Jansson K., Johansen A., 2017, *ApJ*, **834**, 145
- Carrillo J. A., Goudon T., 2004, *J. Sci. Comput.*, **20**, 69
- Cheng Z., Redner S., 1988, *Phys. Rev. Lett.*, **60**, 2450
- Cheng Z., Redner S., 1990, *Journal of Physics A Mathematical General*, **23**, 1233
- Cockburn B., Shu C.-W., 1989, *Mathematics of Computation*, **52**, 411
- Das A., Kumar J., Dosta M., Heinrich S., 2020, *SIAM Journal on Scientific Computing*, **42**, B1570
- Dominik C., Tielens A. G. G. M., 1997, *ApJ*, **480**, 647
- Dominik C., Paszun D., Borel H., 2016, arXiv e-prints,
- Draine B. T., 2004, *Astrophysics of Dust in Cold Clouds*. p. 213, doi:10.1007/3-540-31636-1_3
- Draine B. T., Weingartner J. C., 1996, *ApJ*, **470**, 551
- Dullemond C. P., Dominik C., 2005, *A&A*, **434**, 971
- Ernst M. H., Pagonabarraga I., 2007, *Journal of Physics A Mathematical General*, **40**, F331
- Filbet F., Laurençot P., 2004, *SIAM Journal on Scientific Computing*, **25**, 2004
- Friedlander S. K., et al., 2000, *Smoke, dust, and haze*. Vol. 198, Oxford university press New York
- Gonzalez J. F., Laibe G., Maddison S. T., 2017, *MNRAS*, **467**, 1984
- Goudon T., Lagoutière F., Tine L. M., 2013, *Mathematical Models and Methods in Applied Sciences*, **23**, 1177
- Gould R. J., Salpeter E. E., 1963, *ApJ*, **138**, 393
- Håkansson A., Trägårdh C., Bergenståhl B., 2009, *Chemical Engineering Science*, **64**, 2915
- Hidy G., Brock J., 1972, *Topics in Current Aerosol Research. International Reviews in Aerosol Physics and Chemistry*, Pergamon, doi:https://doi.org/10.1016/B978-0-08-016809-8.50001-2
- Hirashita H., Yan H., 2009, *MNRAS*, **394**, 1061
- Hirashita H., Il’in V. B., Pagani L., Lefèvre C., 2021, *MNRAS*, **502**, 15
- Hoang T., 2019, *ApJ*, **876**, 13
- Jaupart E., Laibe G., 2020, *MNRAS*, **492**, 4591
- Jones A. P., 2004, in Witt A. N., Clayton G. C., Draine B. T., eds, *Astronomical Society of the Pacific Conference Series Vol. 309, Astrophysics of Dust*. p. 347
- Jones A. P., 2021, arXiv e-prints, p. arXiv:2111.04509
- Kenyon S. J., Bromley B. C., 2004, *AJ*, **127**, 513

- Khain A. P., Pinsky M., 2018, Physical processes in clouds and cloud modeling. Cambridge University Press, doi:10.1017/9781139049481
- Kobayashi H., Tanaka H., 2010, *Icarus*, 206, 735
- Kostoglou M., 2007, in Salman A. D., Ghadiri M., Hounslow M. J., eds, Particle Breakage, Vol. 12, Handbook of Powder Technology. Elsevier Science B.V., pp 793–835, doi:10.1016/S0167-3785(07)12021-2
- Kostoglou M., Karabelas A. J., 2000, *Journal of Physics A Mathematical General*, 33, 1221
- Kumar J., 2007, PhD thesis, Otto-von-Guericke-Universität Magdeburg, doi:10.25673/4837
- Kumar R., Kumar J., 2013, *Applied Mathematics and Computation*, 219, 5140
- Kumar R., Kumar J., Warnecke G., 2014, *Kinetic & Related Models*, 7, 713
- Laibe G., Lombart M., 2022, *MNRAS*, 510, 5220
- Lebreuilly U., Hennebelle P., Colman T., Commerçon B., Klessen R., Maury A., Molinari S., Testi L., 2021, *ApJ*, 917, L10
- Lesur G., et al., 2022, arXiv e-prints, p. arXiv:2203.09821
- Leyvraz F., Tschudi H. R., 1981, *Journal of Physics A Mathematical General*, 14, 3389
- Liu H., Gröpler R., Warnecke G., 2019, *SIAM Journal on Scientific Computing*, 41, B448
- Lombart M., Laibe G., 2021, *MNRAS*, 501, 4298
- Mazzarotta B., 1992, *Chemical Engineering Science*, 47, 3105
- McGrady E. D., Ziff R. M., 1987, *Phys. Rev. Lett.*, 58, 892
- Melzak Z., 1957, *Transactions of the American Mathematical Society*, 85, 547
- Müller H., 1928, *Fortschrittsberichte über Kolloide und Polymere*, 27, 223
- Ormel C. W., Paszun D., Dominik C., Tielens A. G. G. M., 2009, *A&A*, 502, 845
- Pagonabarraga I., Kanzaki T., Cruz-Hidalgo R., 2009, *European Physical Journal Special Topics*, 179, 43
- Paszun D., Dominik C., 2009, *A&A*, 507, 1023
- Paul J., Kumar J., 2018, *Mathematical Methods in the Applied Sciences*, 41, 2715
- Price D. J., et al., 2018, *Publ. Astron. Soc. Australia*, 35, e031
- Pruppacher H., Klett J., 2010, *Microstructure of Atmospheric Clouds and Precipitation*. Springer Netherlands, doi:10.1007/978-0-306-48100-0_2
- Ramkrishna D., 2000, *Population balances: Theory and applications to particulate systems in engineering*. Elsevier, doi:10.1016/B978-0-12-576970-9.X5000-0
- Redner S., 1990, *Statistical Theory of Fragmentation*. Springer US, Boston, MA, pp 31–48, doi:10.1007/978-1-4615-6864-3_3
- Safronov V. S., 1972, *Evolution of the protoplanetary cloud and formation of the earth and planets*.
- Srivastava R. C., 1971, *Journal of Atmospheric Sciences*, 28, 410
- Tanaka H., Inaba S., Nakazawa K., 1996, *Icarus*, 123, 450
- Testi L., et al., 2014, *Protostars and Planets VI*, p. 339
- Weidenschilling S. J., 1977, *MNRAS*, 180, 57
- Whipple F. L., 1972, in Elvius A., ed., *From Plasma to Planet*. p. 211
- Williams D. R., Wetherill G. W., 1994, *Icarus*, 107, 117
- Wolfram Research I., 14, *Mathematica*, Version 14.0, <https://www.wolfram.com/mathematica>
- Youdin A. N., Goodman J., 2005, *ApJ*, 620, 459
- Zhang X., Shu C.-W., 2010, *Journal of Computational Physics*, 229, 3091
- Ziff R. M., McGrady E. D., 1985, *Journal of Physics A Mathematical General*, 18, 3027
- da Costa F. P., 2015, in Bourguignon J.-P., Jeltsch R., Pinto A. A., Viana M., eds, *Mathematics of Energy and Climate Change*. Springer International Publishing, Cham, pp 83–162, doi:10.1007/978-3-319-16121-1_5

APPENDIX A: LINEAR FRAGMENTATION

The linear fragmentation model is a fragmentation process in which the breakup of grains is driven spontaneously by external forces where dust collisions are rare, meaning that the fragmentation is not due to grain-grain collisions (Cheng & Redner 1990; Kostoglou

& Karabelas 2000). Linear fragmentation is an ubiquitous phenomenon in nature that underlies processes such as polymer degradation (Ziff & McGrady 1985), breakup of liquid droplets (Pruppacher & Klett 2010; Khain & Pinsky 2018), grinding or crushing of rocks (Austin 1971), industrial crystallisation (Mazzarotta 1992), emulsification (Ramkrishna 2000; Håkansson et al. 2009) and disruption of grains (Draine & Weingartner 1996; Hoang 2019). Similar to the Smoluchowski coagulation equation (Müller 1928; Safronov 1972), the linear fragmentation equation is formalised by a deterministic mean-field approach (Redner 1990). With no known generic analytic solutions, a large literature exists concerning the linear fragmentation equation since the 1950s (Melzak 1957; Srivastava 1971; Ziff & McGrady 1985; Redner 1990; Kostoglou 2007; Kumar & Kumar 2013; Banasiak et al. 2019).

A1 Conservative form

The linear fragmentation equation was formalised in a mean-field approach by Melzak (1957). The by-products of fragmenting aggregates are called fragments and are assumed to be spherical. Spatial correlations are neglected. For physical systems involving the fragmentation of aggregates made of a large number of monomers, it is convenient to assume a continuous mass distribution. The population density of grains within a differential mass range dm is characterised by its number density $n(m)$. The continuous linear fragmentation equation is given by

$$\frac{\partial n(m, t)}{\partial t} = -a(m)n(m, t) + \int_m^{\infty} b(m, m')a(m')n(m', t)dm', \quad (\text{A1})$$

where t denotes time, $n(m, t)$ is the number density function per unit mass for particles of mass m . The first term on the right-hand side of Eq. A1 accounts for the loss of particles of mass m due to their breaking up into smaller particles (breaking of an orange particle on Fig. A1), the coefficient $a(m)$ being the rate of fragmentation for particles of mass m . The second term of Eq. A1 represents the increase of particles of mass m produced by the fragmentation of a particle of mass $m' > m$ (left side on Fig. A1), the coefficient $b(m, m')$ being the distribution of fragments.

If $n_0(m) = n(m, 0)$, is the initial number density distribution per unit mass, then the total mass density, the total number density of grains and the mean mass of the initial distribution can be written as

$$M = \int_0^{\infty} mn_0(m)dm, \quad N_0 = \int_0^{\infty} n_0(m)dm, \quad m_0 = \frac{M}{N_0}. \quad (\text{A2})$$

The linear fragmentation equation is written in dimensionless form by using the following dimensionless variables (Kostoglou 2007):

$$\begin{cases} x \equiv m/m_0, & y \equiv m'/m_0, & \tau = a(m_0)t, \\ \tilde{a}(x) = a(m)/a(m_0), & \tilde{b}(x, y) = m_0b(m, m'), \\ f(x, \tau) = m_0 n(m, t)/N_0. \end{cases} \quad (\text{A3})$$

Here, $a(m_0)$ is a normalising constant with dimension $[s^{-1}]$. We use the variables x , τ , and f for the dimensionless mass, time, and number density, respectively, to be consistent with the existing literature (e.g. Kostoglou 2007; Banasiak et al. 2019) such that Eq. A1

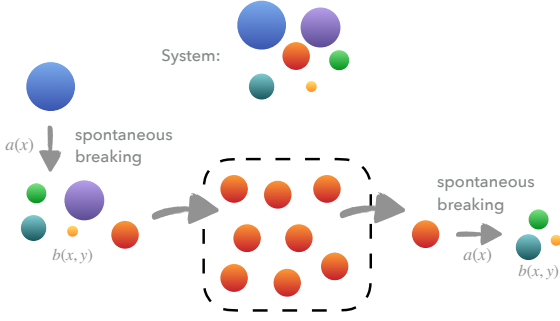


Figure A1. Scheme of the spontaneous fragmentation equation Eq. A1. The number density of orange grains, mass m , increases due to fragmentation of the blue grains with mass greater than m , and decreases due to fragmentation of orange grains.

writes

$$\frac{\partial f(x, \tau)}{\partial \tau} = -\tilde{a}(x)f(x, \tau) + \int_x^\infty \tilde{b}(x, y)\tilde{a}(y)f(y, \tau)dy. \quad (\text{A4})$$

Kumar (2007) has shown that Eq. A4 can be equivalently written in conservative form, as follows

$$\begin{cases} \frac{\partial g(x, \tau)}{\partial \tau} + \frac{\partial F_{\text{frag}}[g](x, \tau)}{\partial x} = 0, \\ F_{\text{frag}}[g](x, \tau) = - \int_0^\infty \int_0^x u\tilde{b}(u, v)\frac{\tilde{a}(v)}{v}g(v, \tau)dudv, \end{cases} \quad (\text{A5})$$

where $g(x, \tau) \equiv xf(x, \tau)$ is the mass density of grains per unit mass, and $F_{\text{frag}}[g](x, \tau)$ is the flux of mass density across the mass x triggered by fragmentation.

A2 Discontinuous Galerkin algorithm

Similar to the non-linear fragmentation equation, the Discontinuous Galerkin method is applied to the linear fragmentation (Liu et al. 2019; Lombart & Laibe 2021) and tested against the exact solutions (Ziff & McGrady 1985). Performances of the DG scheme are similar to the application on the non-linear fragmentation and only a result for the linear fragmentation $a(x) = x$ with 20 bins is shown here in Fig. A2 for example.

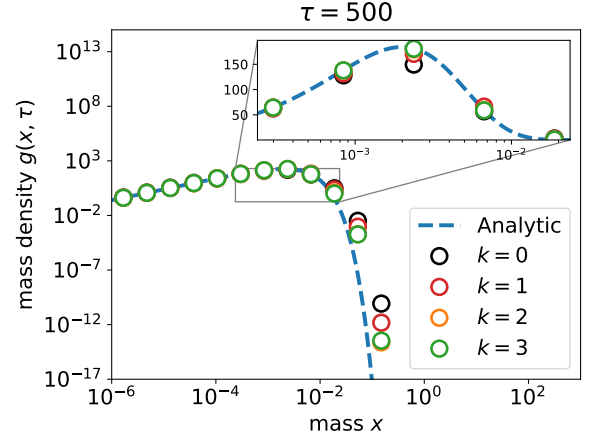


Figure A2. Test for the linear fragmentation rate with $N = 20$ bins. Numerical solution $p_j(x, \tau)$ evaluated with the geometric mean \hat{x}_j over each bin I_j . A zoom-in of the peak of the distribution shows that an absolute error of $\sim 0.1 - 1\%$ is reached with $k = 1, 2, 3$, compared to 20% obtained with $k = 0$. Accuracy in the exponential tail is improved by a factor 1000 with $k = 3$ compared to $k = 0$. The missing points have values below 10^{-17} .

APPENDIX B: CONSTANT COLLISION KERNEL

The derivation of Eq. 14 is given here:

$$\begin{aligned} \frac{dN}{dt} &= -N^2 + N \int_0^\infty \int_x^\infty \frac{b(x/y)}{y} f(y, t) dy dx \\ &= -N^2 + N \int_0^\infty \int_0^\infty H(y-x) \frac{b(x/y)}{y} f(y, t) dy dx \\ &= -N^2 + N \int_0^\infty \int_0^\infty \underbrace{H(y-x)}_{\text{applied on } x} \frac{b(x/y)}{y} f(y, t) dx dy \\ &= -N^2 + N \int_0^\infty \int_0^y \frac{b(x/y)}{y} f(y, t) dx dy \\ &\stackrel{w \equiv x/y}{=} -N^2 + N \int_0^\infty \int_0^1 b(w) f(y, t) dw dy \\ &= (b_0 - 1)N^2, \end{aligned} \quad (\text{B1})$$

where H is the Heaviside function and $b_0 = \int_0^1 b(w)dw$, with $w = x/y$.

APPENDIX C: CFL CONDITION

The conservative form of the linear fragmentation writes (Kumar et al. 2014; Liu et al. 2019)

$$\begin{cases} \frac{\partial g(x, \tau)}{\partial \tau} + \frac{\partial F_{\text{linfrag}}[g](x, \tau)}{\partial x} = 0, \\ F_{\text{linfrag}}[g](x, \tau) = - \int_0^\infty \int_0^x ub(u, v)\frac{a(v)}{v}g(v, \tau)dudv, \end{cases} \quad (\text{C1})$$

where $a(v)$ is the rate of fragmentation for particle of mass v and $b(u, v)$ is the distribution of fragments of mass u resulting from a break-up of particle of mass v . The DG scheme applied to Eq.C1 for order 0 writes

$$g_j^{0, n+1} = g_j^{0, n} - \frac{\Delta \tau}{\Delta x_j} [F_{\text{linfrag}}(x_{j+1/2}, \tau) - F_{\text{linfrag}}(x_{j-1/2}, \tau)], \quad (\text{C2})$$

where

$$F_{\text{linfrag}}(x_{j+1/2}, \tau) = - \sum_{l=j+1}^N \int_{I_l} \int_{x_{\min}}^{x_{j+1/2}} ub(u, v) \frac{a(v)}{v} g_l^0(\tau) dudv, \quad (\text{C3})$$

which is the numerical representation of the flux (Liu et al. 2019). Therefore, we obtain

$$\begin{aligned} & F_{\text{linfrag}}(x_{j+1/2}, \tau) - F_{\text{linfrag}}(x_{j-1/2}, \tau) \\ &= - \sum_{l=j+1}^N \int_{I_l} \int_{x_{\min}}^{x_{j+1/2}} ub(u, v) \frac{a(v)}{v} g_l^0(\tau) dudv \\ &\quad + \sum_{l=j}^N \int_{I_l} \int_{x_{\min}}^{x_{j-1/2}} ub(u, v) \frac{a(v)}{v} g_l^0(\tau) dudv \\ &= - \sum_{l=j+1}^N \int_{I_l} \int_{x_{\min}}^{x_{j-1/2}} ub(u, v) \frac{a(v)}{v} g_l^0(\tau) dudv \\ &\quad - \sum_{l=j+1}^N \int_{I_l} \int_{x_{j-1/2}}^{x_{j+1/2}} ub(u, v) \frac{a(v)}{v} g_l^0(\tau) dudv \\ &\quad + g_j^0(\tau) \int_{I_j} \int_{x_{\min}}^{x_{j-1/2}} ub(u, v) \frac{a(v)}{v} dudv \\ &\quad + \sum_{l=j+1}^N \int_{I_l} \int_{x_{\min}}^{x_{j+1/2}} ub(u, v) \frac{a(v)}{v} g_l^0(\tau) dudv. \end{aligned} \quad (\text{C4})$$

By simplifying Eq. C4,

$$\begin{aligned} & F_{\text{frag}}(x_{j+1/2}, \tau) - F_{\text{frag}}(x_{j-1/2}, \tau) \\ &= g_j^0(\tau) \int_{I_j} \int_{x_{\min}}^{x_{j-1/2}} ub(u, v) \frac{a(v)}{v} dudv \\ &\quad - \sum_{l=j+1}^N \int_{I_l} \int_{x_{j-1/2}}^{x_{j+1/2}} ub(u, v) \frac{a(v)}{v} g_l^0(\tau) dudv. \end{aligned} \quad (\text{C5})$$

Eq. C2 writes

$$\begin{aligned} g_j^{0,n+1} &= g_j^{0,n} \left(1 - \frac{\Delta\tau}{\Delta x_j} \int_{I_j} \int_{x_{\min}}^{x_{j-1/2}} ub(u, v) \frac{a(v)}{v} dudv \right) \\ &\quad + \frac{\Delta\tau}{\Delta x_j} \sum_{l=j+1}^N \int_{I_l} \int_{x_{j-1/2}}^{x_{j+1/2}} ub(u, v) \frac{a(v)}{v} g_l^0(\tau) dudv \\ &\geq g_j^{0,n} \left(1 - \frac{\Delta\tau}{\Delta x_j} \int_{I_j} \int_{x_{\min}}^{x_{j-1/2}} ub(u, v) \frac{a(v)}{v} dudv \right). \end{aligned} \quad (\text{C6})$$

Therefore, to guarantee the positivity of $g_j^{0,n+1} > 0$ at time-step $n + 1$, the CFL condition writes

$$\Delta\tau \sup_j \left(\frac{1}{\Delta x_j} \int_{I_j} \int_{x_{\min}}^{x_{j-1/2}} ub(u, v) \frac{a(v)}{v} dudv \right) < 1. \quad (\text{C7})$$